Nonresonant Confocal Raman Imaging of DNA and Protein Distribution in Apoptotic Cells

N. Uzunbajakava,* A. Lenferink,* Y. Kraan,* E. Volokhina,* G. Vrensen,† J. Greve,* and C. Otto*
*Biomedical Technology Institute, Department of Applied Physics, University of Twente, Enschede, The Netherlands; and
†Department of Ophthalmology, Leiden University Medical Center, Leiden, The Netherlands

ABSTRACT Nonresonant confocal Raman imaging has been used to map the DNA and the protein distributions in individual single human cells. The images are obtained on an improved homebuilt confocal Raman microscope. After statistical analysis, using singular value decomposition, the Raman images are reconstructed from the spectra covering the fingerprint region. The data are obtained at a step interval of ~250 nm and cover a field from 8- to 15-μm square in size. Dwell times at each pixel are between 0.5 and 2 s, depending on the nature and the state of the cell under investigation. High quality nonresonant Raman images can only be obtained under these conditions using continuous wave high laser powers between 60 and 120 mW. We will present evidence that these laser powers can still safely be used to recover the chemical distributions in fixed cells. The developed Raman imaging method is used to image directly, i.e., without prior labeling, the nucleotide condensation and the protein distribution in the so-called nuclear fragments of apoptotic HeLa cells. In the control (nonapoptotic) HeLa cells, we show, for the first time by Raman microspectroscopy, the presence of the RNA in a cell nucleus.

INTRODUCTION

Many cell biological processes, such as cell division, cell differentiation, apoptosis, necrosis, and phagocytosis, are accompanied by large spatial reorganizations of the molecular components that constitute the cell. The chemical composition of the cell too can strongly change over the time. New microscopic techniques reveal the behavior of the molecules in key processes of the cell's existence. Fluorescence microscopic techniques are now becoming sufficiently sensitive to track the individual molecules and in this way contribute to our understanding of cellular processes (Iino et al., 2001; Byassee et al., 2000). External labeling of the molecule of interest by chemical or recombinant methods is so far necessary, as most molecules naturally occurring in a cell cannot, directly, be identified by the methods of fluorescence microscopy. However, the accessibility of the DNA to the external fluorescent dyes markedly depends on a type of the dye and the metabolic state of the cell as well as the phase of cell differentiation. So, DNA in situ is only partially accessible to the external dyes (Darzynkiewicz, 1990), which may introduce uncertainty into data interpretation.

On the other hand, microscopic techniques based on the measurement of the vibrational modes of the molecules are chemically specific and therefore are capable to image directly, i.e., without prior labeling, the chemical composition and the distribution of molecules. The feasibility of resonant Raman scattering (Puppels et al., 1990, 1993a,b; Wood et al., 2001), coherent anti-Stokes Raman scattering (CARS) (Zumbusch et al., 1999; Cheng et al., 2002), and Fourier transform infrared absorption (FTIR) (Diem et al., 2002; Lasch et al., 2002) for cellular imaging have been shown. Single-cell vibrational spectroscopy using nonresonant Raman spectroscopy proved to be sufficiently sensitive to show the typical spectra of the cell nucleus and the cell cytoplasm in human white blood cells (Puppels et al., 1990, 1993a,b). Resonant Raman microspectroscopy of neutrophilic and eosinophilic granulocytes showed very clear fingerprints of the presence of the oxidizing enzymes that these cells require for their functionality (Puppels et al., 1991b; Salmaso et al., 1994; Sijtsema et al., 2000). The activation of these leukocytes and the accompanying changes in the redox states of both myeloperoxidase and cytochrome b558 in neutrophilic granulocytes and eosinophil peroxidase in eosinophilic granulocytes could be shown using resonant Raman microspectroscopy (Puppels et al., 1991b; Sijtsema et al., 1998a, 2000; Otto et al., 1998). Carotenoids in individual living human lymphocytes (Puppels et al., 1993a; Ramanauskaite et al., 1997) gave rise to sufficiently strong resonant Raman scattering that enabled direct Raman imaging of the carotenoid distribution in the cell. The presence and distribution of carotenoids was also shown in living luteal cells (Arikan et al., 2002).

The absorption cross section in the infrared of naturally occurring molecules is sufficiently high to record their distribution. Healthy and cancer cells could be distinguished using the method of FTIR absorption microscopy (Diem et al., 2002). The transmissive mode of this technique (Lasch et al., 2002) and the long wavelengths inherent to this method prevent high resolution image formation, which is required to chemically image the nuclear fragments of apoptotic cells.

So far, the very low scattering cross section of naturally occurring compounds, such as DNA, RNA, proteins, and phospholipids, prevented imaging of their distribution in

Submitted November 7, 2002, and accepted for publication January 28, 2003.

Address reprint requests to Natallia Uzunbajakava, University of Twente, Postbus 217, Enschede, The Netherlands 7500 AE. Tel.: 31-53-489-4612; Fax: 31-53-489-1105; E-mail: n.uzunbajakava@tn.utwente.nl.

© 2003 by the Biophysical Society

0006-3495/03/06/3968/14 $2.00

single cells by nonresonant Raman microscopy. Recently it was shown that by CARS microscopy the low nonresonant scattering cross section is at least partially overcome by high peak powers in the laser beams used to generate the coherent signal (Zumbusch et al., 1999; Volkmer et al., 2001). This was shown both in narrow band mode (Cheng et al., 2001) as well as in a broad band mode (Cheng et al., 2002).

We will show here that by a combination of confocal Raman microscopy and simple data analysis tools, nonresonant Raman images of DNA, RNA, proteins, and phospholipids can be obtained. The advantage of the broad spectral response in spontaneous Raman scattering of $\sim$1900 cm^{-1} compensates for the low photon flux in this process. As a result, simultaneous imaging of the whole relevant fingerprint area can be performed.

We apply the method of nonresonant Raman imaging to investigate the distribution of cytoplasmic and nuclear materials of the cells in a late stage of apoptosis. Apoptosis is a crucial process in the behavior of mammalian cells in many different situations. It was distinguished from necrotic cell death as a specific controlled mechanism by which the cells are eliminated (Kerr et al., 1972). Apoptosis is indispensable during development and tissue remodeling (Schwartz and Osborne, 1993). The cells undergoing apoptosis reveal a specific morphology, some hallmarks of which are cell shrinkage and rearrangement of the cellular organelles, chromatin condensation, nucleolus disintegration, fragmentation of the cell nucleus, and the formation of apoptotic bodies (Kerr et al., 1972, 1994; Wyllie 1992; Majno and Joris, 1995; Compton, 1992; Nagata, 2000). Evidence also exists that DNA-, RNA-, and ribonuclear protein complexes are extruded separately from the cell undergoing apoptosis (Biggiogera et al, 1998; Halicka et al., 2000; Houge et al., 1995). Recent data has shown that DNA and RNA were segregated and packed into different granules, which ultimately formed apoptotic bodies (Halicka et al., 2000).

Here we show for the first time spatially and spectrally resolved nonresonant Raman images of apoptotic HeLa cells, control (nonapoptotic) HeLa cells, and peripheral blood lymphocytes. The DNA-, protein-, and phospholipids distributions in the single apoptotic cell are shown.

MATERIALS AND METHODS

Peripheral blood lymphocytes isolation

Peripheral blood of healthy donors was obtained by venapuncture and collected in heparinized tubes. The peripheral blood lymphocytes (PBLs) were isolated using standard density centrifugation followed by monocyte depletion (Terstappen et al., 1986). A few drops of the PBL suspension in RPMI 1640 medium without phenol red (Seromed, Biochrom KG, Berlin, German, cat. T-127-01), were added onto PLL-coated CaF_2 substrate to form a distribution of single cells. As a substrate for the cells in all Raman experiments, calcium fluoride (CaF_2) disks were used (Schuster et al., 2000). CaF_2 disks were incubated overnight in a solution of 0.01% poly-l-lysine (PLL; cat. P-1274, Sigma Chemical, St. Louis, MO) in phosphate-buffered saline (PBS) at 4°C. The lymphocyte population consists of T-, B-, and K-cells, which were not further separated. Individual round cells were adhered to the surface of the substrate. The cells were typically 20 μm apart. After incubation at 37°C for 30 min, adhered PBLs were fixed in 1% paraformaldehyde. Fixed PBLs were washed 3× in PBS. The cells with the CaF_2 disk were transferred to a petri dish (diameter 3.5 cm) and 3 ml of PBS was added.

HeLa cells culturing and apoptosis induction

HeLa cells were grown on CaF_2 disks at 37°C in an atmosphere containing 5% CO_2 in the Iscove's modified Dulbecco's medium (Gibco Invitrogen, Groningen, Netherlands, cat. 21056-023), supplemented with 10% bovine serum (Sigma-Aldrich Chemie BV, Zwijndrecht, Netherlands, cat. A-7906), 2 mM L-glutamine (Sigma-Aldrich Chemie BV, cat. G-6392), and antibiotic/antimicotic (Gibco Invitrogen, cat. 15240-062). Apoptosis in HeLa cells was induced during incubation with 40 nM taxol (lot 005, Cytoskeleton, Denver, CO), added to the growth medium during 24 h (Yeung et al., 1999). HeLa cells, both apoptotic and control, were fixed in 1% paraformaldehyde followed by three washing steps in PBS before transfer to the Raman microscope.

Fluorescent labeling of cells

Fluorescence imaging was used to develop the method of the induction of apoptosis in HeLa cells. To visualize the DNA distribution in control and apoptotic HeLa cells the DNA dye Hoechst 33342 (cat. H-1399, Molecular Probes, Eugene, OR) was used. The dye preferentially binds to A-T rich regions (Loontiens et al., 1990), and has the maxima of absorption and emission at $\sim$350 and $\sim$460 nm, respectively.

Once fixed, both control and apoptotic cells were incubated for 15 min in 20 μmol solution of Hoechst 33342 in PBS followed by three washing steps in PBS.

The confocal Raman microspectrometer

All Raman measurements were done using a homebuilt confocal Raman microspectrometer (Sijtsema et al., 1998b). A Kr-ion laser (Coherent, Innova 90-K, Santa Clara, CA) provided the excitation wavelength of 647.1 nm. The system was modified and optimized for single-cell nonresonant Raman imaging. Raman images were collected in the following way: during Raman imaging a full spectrum (width $\sim$1900 cm^{-1}) was recorded at each position of the laser beam. Raman images of a single cell in the vibrational band of interest were reconstructed after the measurement. A water immersion objective (Zeiss Plan Neofluar, Carl Zeiss, Thornwood, NY) was used for the acquisition of all Raman spectra and Raman images. A blazed holographic grating with 600 gr/mm (Jobin-Yvon, Paris, France) was used for dispersion, the spectral resolution on the charge-coupled device (CCD) camera was 1.7 cm^{-1}/pixel. The lateral spatial resolution was limited by the diffraction and was 550 nm in the Raman microscope. The definition of the resolution is based on the diameter of the laser beam waist at which the beam intensity has fallen to $1/e^2$ of its peak value. The axial resolution was 2.4 μm with a 25-μm confocal pinhole. As a criterion for the axial resolution, the full width at half-maximum of the intensity profile of the Raman scattering of a thin ($\sim$300-nm) polystyrene layer was used, as it is obtained from an axial scan through the laser focus.

The output power of the laser source during Raman imaging was monitored by a photodiode in synchronicity with the raster scanning in Raman imaging. Laser power fluctuations were observed to be <0.5% during typical image accumulation times of $\sim$10–25 min.

Raman spectra of the cells were recorded with 30 mW laser power and the accumulation times of 60–100 s. Raman images were recorded with laser powers of 100–120 mW and accumulation times of 1–2 s/pixel.

Postregistration processing of the Raman data consisted of the subtraction of the offset of the CCD camera, and a correction for the total setup

frequency dependence by a procedure similar to that used by Puppels and colleagues (Puppels et al., 1991a).

The two-photon fluorescence microscope

The Raman microscope was integrated with a fluorescence microscope that could be used either in one- or two-photon excitation modes. The continuous wave (cw) Kr-ion laser line at 647.1-nm wavelength, that was used in Raman imaging, was also used to excite the two-photon fluorescence (TPE) of the DNA dye Hoechst 33342. The TPE-stage was integrated with the Raman microscope so that rapid change between both imaging modalities was possible. This was obtained by adding a foldable mirror (*M1*; see Fig. 1) (T-mount, Newport, Irvine, CA) after the dichroic beamsplitter. A colored glass filter BG12 (product 03 FCG 013, Melles Griot, Irvine, CA) was used to select the spectral range of interest between 354 and 462 nm (full width at half-maximum of the transmission of the filter) and to suppress the laser light. A lens (focal length, 30 mm) focused the light on the 25-μm confocal pinhole in front of the avalanche photo diode (APD) (EG&G, Optoelectronics, Freemont, CA), used for the registration of the fluorescent signal. Cw-excited two-photon fluorescence images were acquired by scanning an area of 15 $\times$ 15 μm in 128 $\times$ 128 steps with an accumulation time of 1 ms/pixel.

Signal-to-noise ratio estimation

The occurring contrast in Raman images is assessed in terms of the signal-to-noise ratio (S/N). The S/N is defined as the ratio of the intensity of the signal to the standard deviation (SD) of the noise,

$$S/N = I_{\text{signal}}/\sigma_{\text{noise}}, \tag{1}$$

where I_{signal} is the intensity of the signal of interest, and σ_{noise} is the SD of the noise. Four dominant noise components can be distinguished: shot noise, dark current noise, readout noise, and processing noise. In Appendix A, a brief description of these components will be presented.

The independent sources of noise add in quadrature:

$$S/N = \frac{I_{\text{signal}}\eta t}{\sqrt{I_{\text{signal}}\eta t + I_{\text{bk}} + N_{\text{l}}^2 + N_{\text{dc}}^2 + N_{\text{r}}^2}}, \tag{2}$$

where I_{signal} (photons/second) is intensity of the Raman signal before the CCD camera; η (electrons/photon) is CCD quantum efficiency; t (s) is the signal accumulation time; N_{dc} (electron/pixel $\times$ second) is the dark current noise; N_{r} (electron/pixel) is the readout noise; N_{l} is the laser power fluctuation; and I_{bk} is the processing noise. The statistics of the total noise has a Gaussian distribution with a SD sigma (σ_{noise}). All our estimations of the accuracy of the Raman measurements were done in accordance to the Eq. 2 and the specified parameters (Appendix A) for the CCD camera and the light source. On all graphs the interval $[-\sigma, +\sigma]$ is shown as an error bar, which corresponds to a probability of 0.68 to find the signal in the given 2σ interval.

Singular value decomposition

In this work singular value decomposition (SVD; see Golub and van Loan, 1983) was applied to analyze the Raman spectral datasets for two special situations: the evaluation of the potential influence of high laser powers on the chemical distribution of material (Case 1), and the reduction of noise in the image datasets and the subsequent analysis of the spectral content (Case 2).

Case 1

To assess the potential influence of the laser power on the cellular object we have obtained a series of 10 spectra with 10-s acquisition time at one location at a single location in an individual cell. This was repeated using different powers ranging between 10 mW and 140 mW. For each power setting, a matrix (indicated as **A**, see Appendix B) was constructed for the subsequent analysis using SVD. The columns in **A** represent the number of measurements (in the present case, 10). The rows represent the spectral dimension of the signal. Any changes over time can be directly analyzed from the information in the matrix.

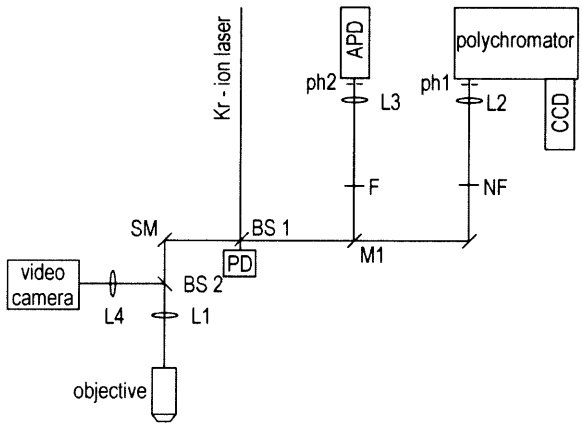

FIGURE 1 Confocal Raman/TPE fluorescent microscope. Both Raman and fluorescent signals were excited with 647.1 nm line of a Kr-ion laser (Innova 90-K, Coherent). The excitation and the detection wavelengths were separated by use of a dichroic beamsplitter (*BS1*) (Chroma Technology). Images were acquired by scanning the sample with a scanning mirror (*SM*) (Leica Lasertechnique GmbH, Heidelberg, Germany). The laser beam, focused by a water immersion objective (Zeiss Plan Neofluar, Carl Zeiss), formed a diffraction-limited spot on the sample. A mobile pellicle beamsplitter (*BS2*) (Melles Griot) was used to visualize the object in white light. White light was focused by a lens (*L4*) (f = 100 mm) on a video camera. A holographic notch filter (*NF*) (Kaiser Optical Systems, Ann Arbor, MI) was used to suppress both reflected and elastically scattered light. A polychromator (Jobin-Yvon, Paris, France) with a blazed holographic grating (600 gr/mm) was used for dispersion. The Raman scattered light was focused on the confocal pinhole (*ph1*) (diameter, 25 μm) at the entrance of the monochromator by a lens (*L2*) (f = 35 mm). Raman signal was detected by a CCD camera (LN/CCD 1100 PB/VISAR, Roper Scientific). The output power of the laser source was monitored by a photodiode (*PD*). A movable mirror (*M1*) (Newport) was used to switch between Raman and fluorescent signal acquisition modes. A colored glass filter (*F*) (Melles Griot) was used to suppress the laser light and to transmit the two-photon excited fluorescence signal. Fluorescent signal was focused on a confocal pinhole (*ph2*) (diameter, 25 μm) by a lens (*L3*) (f = 30 mm) and was detected on an APD (EG&G, Canada, Ltd., Optoelectronics Division).

Case 2

To analyze and spectrally filter the Raman images, we have prepared the matrix (indicated again as **A**, see Appendix B) for the SVD as follows. Raman spectra with the spectral region of interest from 400 to 1800 cm^{-1} were taken. In the matrix **A**, the columns represent the position (x,y) at which a spectrum is obtained, whereas the rows represent the spectral dimension of the signal. The number of singular values is equal to the total number of pixels in the image. However, for our case, not more then 10 singular values were found to have much higher values than all others. The latter ones are associated with orthonormal basis vectors in the matrix **U** (see Appendix B) that were dominated by noise components. After rejection of the corresponding basis vectors, an estimate of the original data matrix (indicated

as $\tilde{\mathbf{A}}$, see Appendix B) was constructed. Starting from this point, Raman images that were reconstructed in a band of interest followed the local baseline correction of the spectral data.

RESULTS

Raman spectral dependence on laser power

Single PBL cells, fixed in 1% paraformaldehyde, were used to investigate the tolerance of the cells for high laser powers at 647.1 nm as well as the dose of the laser radiation that could be applied without causing a change in the Raman spectra of the cells. The experiments were performed on fixed PBL cells that were immersed in the physiological buffer, PBS. Sets of 10 spectra were obtained from a single location inside a cell at a certain laser power. The spectra were analyzed using singular value decomposition (see Appendix B) as it is written in Methods. The singular values, which result from SVD analysis, are presented in Fig. 2, *A–D*, for 10, 30, 70, and 100 mW, respectively. If up to 70 mW of laser power was applied during 100 s, the analysis results in only a single significant singular value. All 10 spectra were identical within the noise level. Starting from 70 mW (Fig. 2 *C*) and progressively increasing at 100 mW (Fig. 2 *D*), a second singular value becomes apparent. It is concluded that laser powers up to 70 mW during 100 s at a single position in a cell do not induce noticeable changes in the Raman spectrum. For all subsequent spectroscopic measurements 30 mW of laser power during 100 s was used. For the Raman imaging measurements, 100 mW of laser power during 0.5–2 s accumulation time, per pixel, was used.

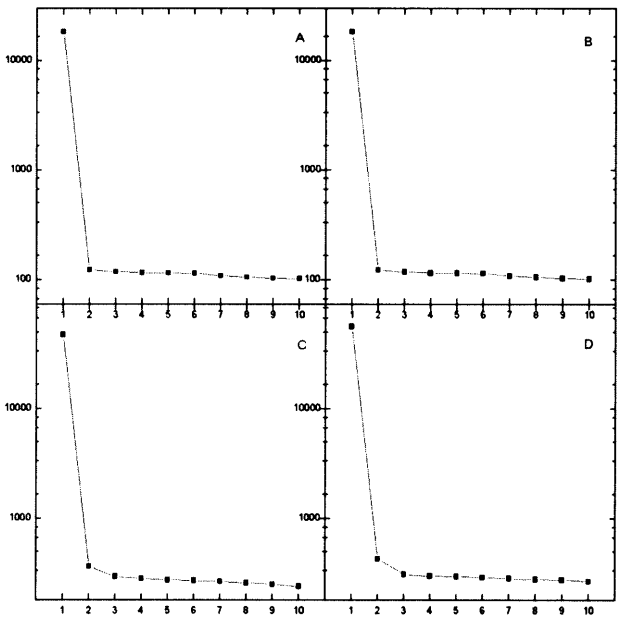

FIGURE 2 Semilogarithmic plots of the singular values of 10 consecutive spectra obtained at a single location in the cell nucleus. The measurement time for each spectrum was 10 s. Results are shown for four different powers: (*A*) 10 mW; (*B*) 30 mW; (*C*) 70; and (*D*) 100 mW. It is observed that the spectra are dominated by a single spectral component. Starting from 70 mW, a very small additional component can be observed that is further increased at higher laser powers.

Raman imaging

Typical Raman spectra measured at a randomly selected location inside the nucleus of a PBL cell are given in Fig. 3, *A* and *B*. Fig. 3 *A* shows the fingerprint region from 700 to 1800 cm^{-1}. Fig. 3 *B* shows the high frequency region that is characteristic for the C-H, N-H, and O-H stretching vibrations. All distinguishable maxima can be assigned (Hayashi et al., 1986; Thomas et al., 1977).

Previously we have reported Raman images of the protein distribution on the basis of the high frequency part of the spectrum (Uzunbajakava et al., 2003). It was shown that the protein distribution in fully maturated PBL cells is completely different from that in actively-transcribing eye lens epithelial cells. The detectable number of counts for the high frequency protein band ($\sim$2900 cm^{-1}) is 4–5$\times$ higher than the corresponding band ($\sim$1451 cm^{-1}) in the fingerprint region.

Here we present a direct comparison of the Raman images of the protein distribution in PBL cells on the basis of the high (Fig. 4 *A*) and low (Fig. 4 *B*) frequency spectral information. The high frequency Raman image of the protein distribution was constructed from the whole band between 2800 cm^{-1} and 3030 cm^{-1}. Two lines are drawn to indicate this region of the spectrum in Fig. 3 *B*. The fingerprint Raman image of the protein distribution was constructed from the spectral region from 1433 cm^{-1} to 1481 cm^{-1}. The correlation coefficient (van der Heijden, 1994) of the high frequency (Fig. 4 *B*) and low frequency (Fig. 4 *A*) protein images was 0.98, confirming the near identity of the data.

Raman images of the DNA and the protein distributions in the nucleus of a single fixed PBL cell were made using the spectral information of the fingerprint region. Fig. 5 *A* shows the Raman image of the DNA distribution in a PBL cell. The Raman band with a maximum $\sim$788 cm^{-1} (spectral region from 774 cm^{-1} to 805 cm^{-1}) was used to construct the Raman image. This band is a nucleotide marker band in the Raman spectrum, to which a number of vibrational modes contribute.

Most dominant contributions are from the complex vibration of the 5′C-O-P-O-C3′ network (Deng et al., 1999) and the cytosine ring breathing mode. Thymine, present in DNA, and uracil, present in RNA, also contribute to this band (Peticolas et al., 1987). Hence, both DNA and RNA will contribute to the Raman scattering in the spectral region $\sim$788 cm^{-1}. A well-known Raman marker band for A-type helices in RNA is located $\sim$813 cm^{-1}. This marker band could not be discerned in PBL cells. This is in agreement with the nature of PBL cells as a terminally differentiated cell in which nucleoli are only occasionally present (Zucker-Franklin et al., 1988). It is concluded that in

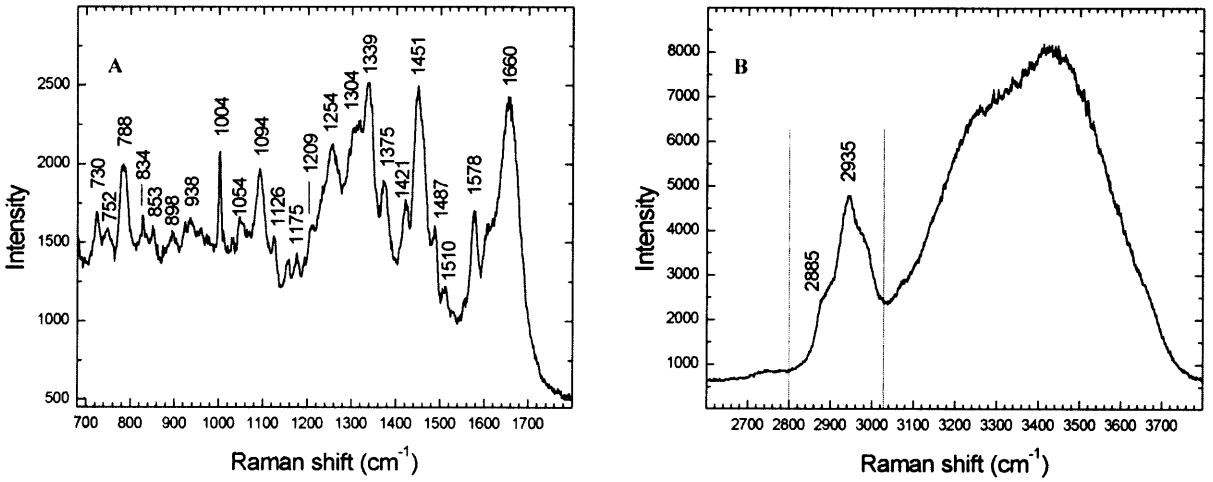

FIGURE 3 Raman spectra of the nuclei of single fixed PBLs. (*A*) The fingerprint region of the spectrum. (*B*) The high frequency region of the spectrum. The cells were adhered to CaF_2 disk, which was immersed in PBS buffer. The laser power was 30 mW, and the accumulation time was 60 s.

PBL cells the Raman band at 788 cm^{-1} represents mainly DNA present in the cell nucleus.

The line profile through the image of the DNA distribution in the PBL nucleus is shown in Fig. 5 *C* with the error bar indicating the SD as $[-\sigma, +\sigma]$ interval as it is written in Methods. The arrow (Fig. 5 *A*) indicates the position in the cell nucleus corresponding with the line profile.

The protein Raman marker band ~1451 cm^{-1} (spectral region from 1431 cm^{-1} to 1481 cm^{-1}) is used to represent the integral protein distribution. The intensity of this band is insensitive to protein secondary structure and depends only on the number of protein CH_2 and CH_3 groups (Tu, 1982; Thomas et al., 1983). Fig. 5 *B* shows the Raman image of the protein distribution in the same PBL cell of Fig. 5 *A*. The line profile through the image of the protein distribution is shown in Fig. 5 *D*, again with the error bar indicating the $[-\sigma, +\sigma]$ interval. The arrow (Fig. 5 *B*) indicates the position in the cell nucleus corresponding with the line profile.

Both the DNA and protein images show considerable variations in the spatial distributions of both materials. Although a clear correspondence in the DNA- and protein distribution can be observed, the images also directly show that the variation in the DNA distribution is much more pronounced than the variation in the protein distribution. The intensity of the selected protein signal is in general higher than that of the selected DNA marker band, thus giving a higher accuracy of the measurements. This is also apparent from the error margins in Fig. 5, *C* and *D*.

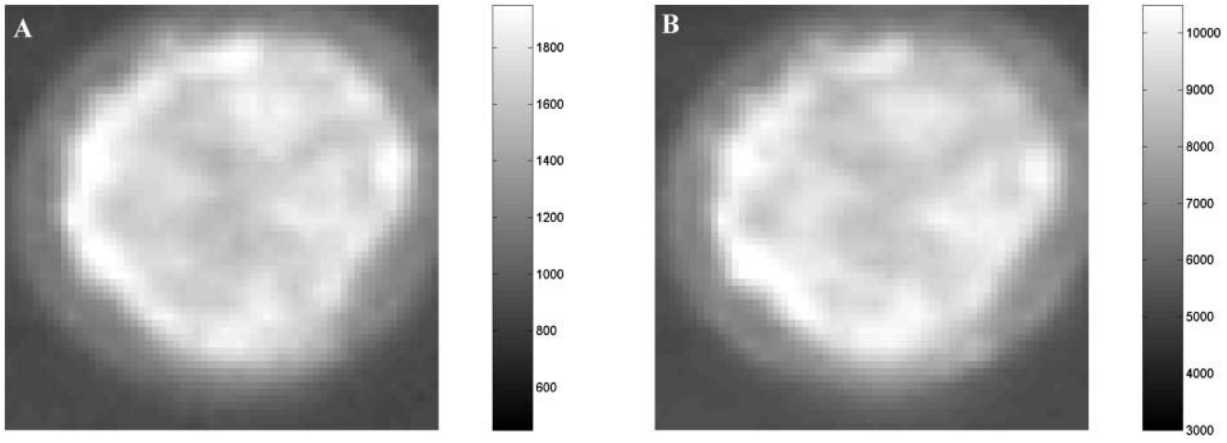

FIGURE 4 Raman images of the protein distribution in a single fixed PBL cell. (*A*) Image made in the 1449 cm^{-1} (spectral region from 1433 cm^{-1} to 1481 cm^{-1}) band. (*B*) In the high frequency band ~2880 cm^{-1} (spectral region from 2800 cm^{-1} to 3030 cm^{-1}). Raman images *A* and *B* were acquired simultaneously. The pixels on the CCD camera along the spectral dimension were hardware-binned in groups having a size of 5 pixels. The spectral resolution of the superpixel was 8.5 cm^{-1}. The camera offset was subtracted. The scanning area was 8 μm × 8 μm. Laser power was 120 mW, and the acquisition time was 1 s per step.

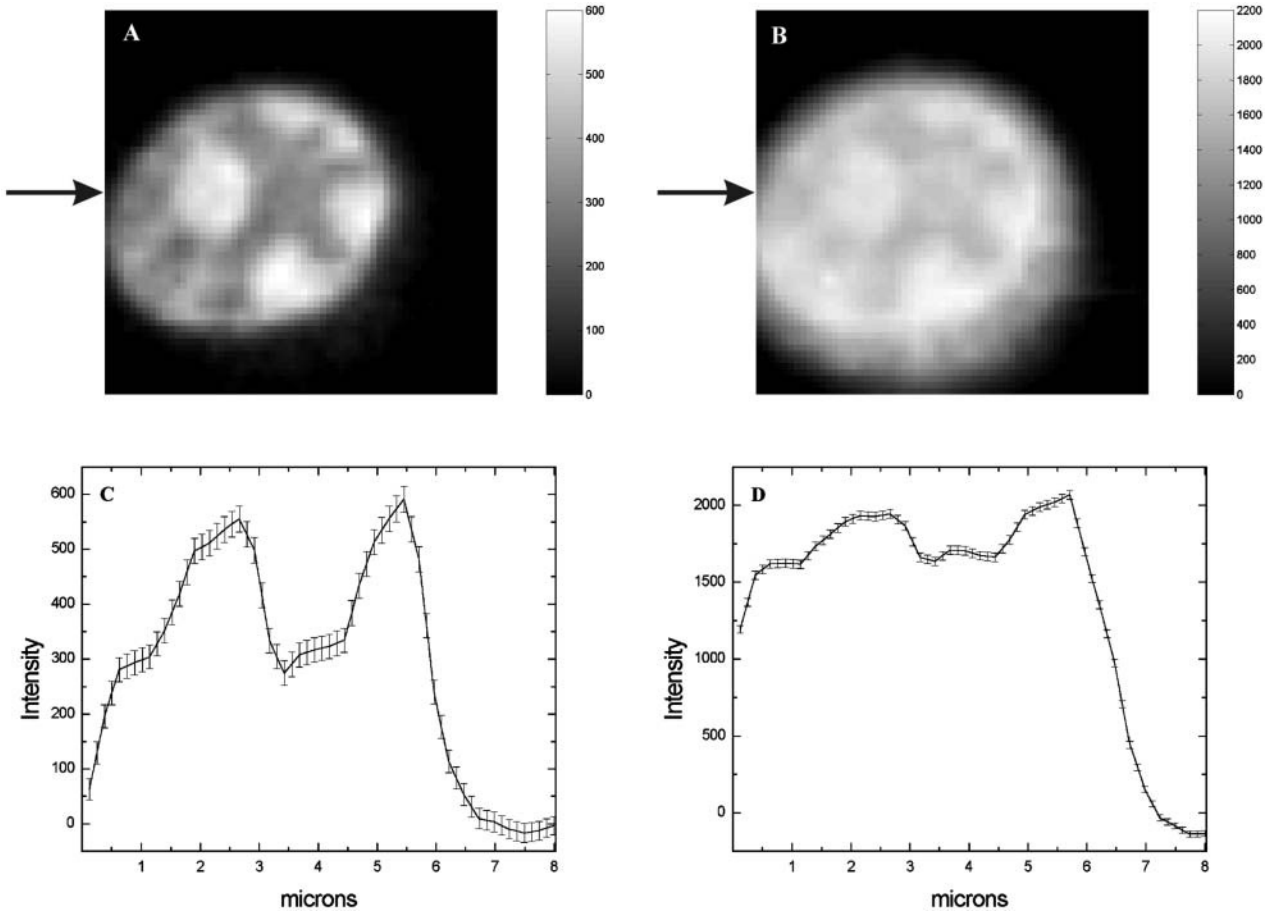

FIGURE 5 Raman images of a single fixed PBL cell on a CaF_2 substrate, immersed in PBS buffer. (*A*) The DNA/RNA image, reconstructed in the 788 cm^{-1} band (spectral region from 774 cm^{-1} to 805 cm^{-1}). (*B*) The protein image, reconstructed in 1451 cm^{-1} band (spectral region from 1431 cm^{-1} to 1481 cm^{-1}). (*C* and *D*) The line profiles with the SDs through the DNA- and protein image, respectively. The SD intervals are shown as 2σ interval and were calculated using Eq. 2. The background intensity due to water and the camera offset was subtracted. The scanning area was 8.4 μm $\times$ 8.4 μm. The laser power was 100 mW, and the acquisition time was 2 s per step.

In a later stage of apoptosis, condensation of DNA and a breakdown of the nucleus take place (Robertson et al., 2000; Compton, 1992; Nagata, 2000). Our method of Raman imaging, described above for the case of PBL cells, was used to visualize the chemical distribution of DNA, RNA, and protein in apoptotic cells. HeLa cells were chosen as a model system. Apoptosis in HeLa cells was induced by treatment with taxol as was described in the Materials section. The method of the induction of apoptosis was refined before the Raman experiments. Continuous wave two-photon fluorescence excitation was used (Hell et al., 1998; Kirsch et al., 1998). The effect of the exposure of HeLa cells to taxol was studied by staining the DNA with the fluorescent dye Hoechst 33342. Cw-two-photon images of the Hoechst 33342 distribution in HeLa cells (control) and HeLa cells treated with taxol were compared.

The DNA distribution in the nucleus of the control HeLa cell and the corresponding white light image of the cell are shown in Fig. 6, *A* and *B*. The scanning area was 15 $\times$ 15 μm and is indicated in the bright light image by the superimposed dashed square. In general the control HeLa cells can be as large as ~60 μm and ~15 μm along the long and short axes of the cell respectively. The control cells are flat and strongly adhered to the surface of the substrate on which they were grown. The variations in the fluorescence intensity of Hoechst 33342 are due to variations in the DNA distribution in the HeLa cell nucleus (Verschure et al., 1999).

Apoptotic cells were easily selected on the basis of typical morphological characteristics. Apoptotic cells shrink to small dimensions. The white light image of such an apoptotic HeLa cell is shown in Fig. 7 *A*. The cell has a size of ~12 μm and is much smaller than the control cell (Fig. 6 *A*). To visualize the spatial distribution of Hoechst 33342-labeled DNA in the apoptotic cell, several fluorescent images were made from different confocal planes in the object. Four of the confocal images are shown in Fig. 7, *B–E*, each obtained 2-μm apart. It is directly observed from the Hoechst 33342 distribution that the nucleus of the apoptotic cell is frag-

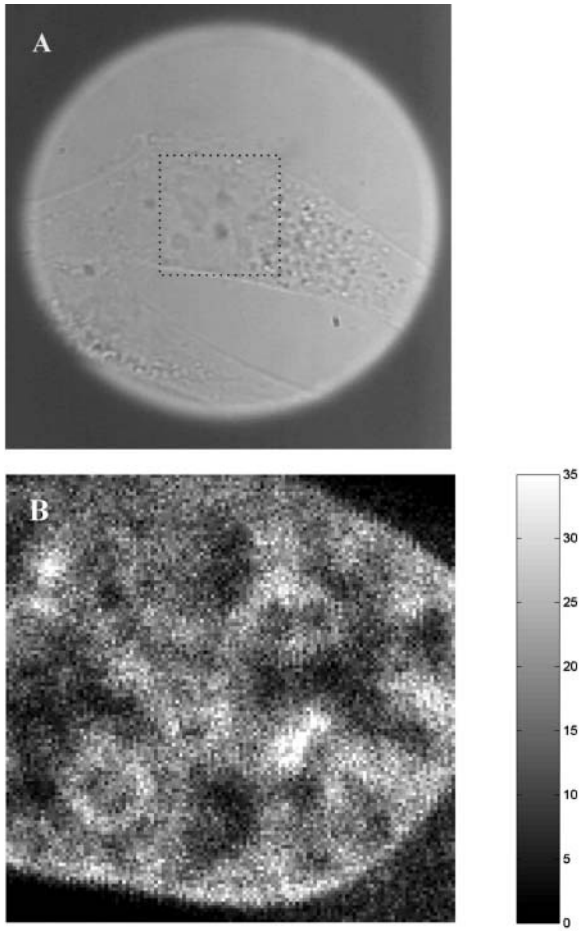

FIGURE 6 (*A*) A white light image of a control HeLa cell. (*B*) The DNA distribution as obtained by two-photon excitation of the DNA dye, Hoechst 33342. The signal is detected on the APD. The color scale is given in counts, detected on the APD. The scanning area was 15 μm × 15 μm in 128 × 128 steps. The cw-laser power was 100 mW, and the accumulation time was 1 ms/pixel.

mented. All apoptotic samples for Raman imaging were prepared using the same method.

The HeLa cells were also spectroscopically characterized. Raman spectra at randomly selected positions inside the cytoplasm and the cell nucleus of the control HeLa cell were acquired (Fig. 8).

Fig. 8 *A* shows a typical Raman spectrum of the nucleus of a control HeLa cell. The spectrum is an average of seven individual spectra, which were all very similar.

The Raman spectrum of the cytosol of the HeLa cell is shown in a Fig. 8 *B*. Its major contributors are proteins and water. A bright light image of a control HeLa cell (Fig. 6 *A*) reveals many submicron-size vesicles in the cytosol. An average of five Raman spectra from such vesicles is shown in Fig. 8 *C*. The most prominent bands are assigned to phospholipids (Tu, 1982). The presence of the band ~1656 cm^{-1} indicates the presence of *C=C* stretch vibrations in the phospholipid spectrum, while the position of a band at 1740 cm^{-1} indicates the presence of carbonyl (*C=O*) stretching bands. The intense phospholipid spectrum of the vesicles suggests that these organelles form part of the endosomal system. The endosomal system is known to play a role as a mediator in membrane transport processes (Lim et al., 2001).

Single cell Raman microspectroscopy of HeLa cells shows that DNA, protein, and phospholipids are the dominant chemical compounds that contribute to the spectra from this type of cell at an excitation wavelength of 647.1 nm. Raman imaging was performed on control HeLa cells to map the distribution of DNA, protein, and phospholipids in cells.

A white light image of a control HeLA cell is shown in Fig. 9 *A*. The marked area was selected for Raman imaging. The nucleotide distribution in this control HeLa cell was imaged using the nucleotide marker band ~788 cm^{-1} (spectral region from 776 cm^{-1} to 805 cm^{-1}; see Fig. 9 *B*). In general the Raman photon flux (photons/s) from the band ~788 cm^{-1} in a HeLa cell is more than 6× lower than in the measurements on PBL cells (Fig. 5 *A*). This is a direct consequence of the much larger size of the nuclei of HeLa cells and the degree of compaction of chromatin inside the PBL nuclei (Uzunbajakava et al., 2003). Fig. 9 *D* shows the DNA distribution along a line, indicated by an arrow in Fig. 9 *B*, through the nucleus and the corresponding SD (2σ interval) in each point.

The Raman image of the protein distribution in the nucleus of the same HeLa cell was reconstructed from the protein marker band ~1451 cm^{-1} (spectral region from 1431 cm^{-1} to 1473 cm^{-1}; see Fig. 9 *C*). In Fig. 9 *E*, a line profile through the image (indicated by an *arrow* in a Fig. 9 *C*) of the protein distribution with the corresponding SD is presented.

The Raman images of the nucleotide- and protein distributions show that a colocalization occurs in certain areas. This can partially be understood from general knowledge of the structure and composition of the chromatin. The chromatin is formed mainly by structural proteins of which the nucleosome core particles and Histon protein H1 are the most abundant. The weight ratio of nucleotides and histone proteins is 1:1. The rest mass of the nucleolar proteins is due to functional proteins, necessary to carry out specific cellular tasks such as translation, DNA repair, etc.

Alternatively, however, it could be that some of the lighter areas in the Raman image belong to the multiple nucleoli present in the nucleus of a HeLa cell. The main components of the nucleoli are rDNA, protein, and rRNA (Dundr and Misteli, 2001). An analysis of the spectral information from high intensity areas and low intensity areas is shown in Fig. 10. The spectrum of region *A* (*high intensity areas*) is an average of the spectra from 41 pixels (Fig. 10 *A*). The spectrum of region *B* (*low intensity areas*) is an average of the spectra from 103 pixels (Fig. 10 *B*). The difference spectrum (region *A* minus region *B*) is presented in Fig. 10 *C*, on a vertical scale that is expanded 6.4×. The selection of

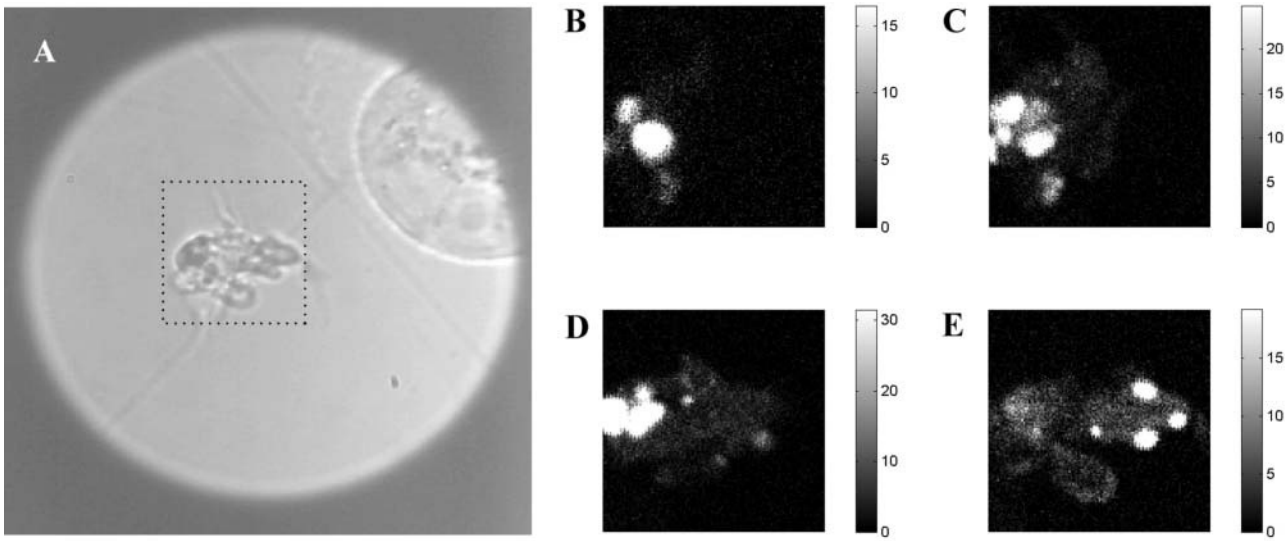

FIGURE 7 The DNA distribution in an apoptotic HeLa cell. (*A*) White light image of an apoptotic HeLa cell. (From *B–E*) The DNA distribution as obtained by two-photon excitation of the DNA marker, Hoechst 33342. Optical sections are made at the different *z*-positions ($\Delta z = 2\ \mu$m) inside the cell. The scanning *x-y* range was 15 μm $\times$ 15 μm in 128 $\times$ 128 steps. The cw-laser power was 100 mW, and the accumulation time was 1 ms/pixel. Each image was scaled from '0' to the 30% of the maximum intensity.

the pixels was guided by the Raman image reconstructed from the band at 788 cm^{-1}. The Raman difference spectrum is dominated by strong bands, which, in position and in intensity distribution, show a high degree of similarity with previously reported nucleotide spectra (Hartman and Thomas, 1985). This is especially notable in the bands at 728 cm^{-1} (adenine ring stretching mode), at 785 cm^{-1} (cytosine- and uracil ring stretching modes), at 813 cm^{-1} (RNA phosphate-sugar marker band), and at 1100 cm^{-1} (symmetric O-P-O stretching vibration), typical for A-type nucleotide helices. In the single-bond stretching region, between 1180 cm^{-1} and 1400 cm^{-1} a pattern of bands is present that are typical for nucleotides. Protein contributions also contribute to the spectrum, most notably at 1004 cm^{-1} (phenylalanine), 1451 cm^{-1} (CH_2/CH_3 bending vibrations), and $\sim$1650 cm^{-1} (amide-I backbone vibrations). The protein contributions are minor, however, if compared with their contributions to the original spectra in Fig. 10, *A* and *B*. It is also known that no A-helical DNA is present in chromatin samples (Thomas et al., 1977; Puppels et al., 1994). We conclude from the Raman image in Fig. 9 *B* and the corresponding spectral data that the bright areas contain RNA, and the dark areas either do not contain RNA, or else contain it at a concentration below the detection threshold. On this basis we assign the bright areas (Fig. 9 *B*) to the nucleoli.

The Raman image of the protein distribution (Fig. 9 *C*) shows, at the periphery of the nucleus, intense bright spots (marked by *arrowheads* in Fig. 9 *C*). The Raman spectra from the corresponding pixels at these regions have a strong similarity with the Raman spectrum obtained from the phospholipid-containing vesicles (Fig. 8 *C*). The relatively intense and narrow band at 1440 cm^{-1} in the vesicles spectrum has a strong overlap with the 1451 cm^{-1} band, used for protein image reconstruction. It is concluded that some care has to be taken, in mixed phospholipid-protein systems, in the use of the band $\sim$1450 cm^{-1} as a marker band for just the protein distribution.

Raman images of the nucleotide- and protein distribution in an apoptotic HeLa cell are given in Fig. 11, *B* and *C*, respectively. A white light image of the HeLa cell is shown in Fig. 11 *A*. The nucleotide Raman image is reconstructed from the band $\sim$788 cm^{-1} (spectral region from 774 cm^{-1} to 805 cm^{-1}). Several nucleotide-containing fragments of the cell nucleus can be clearly distinguished. The size of the nuclear fragments is in the order of 1–4 μm. The intensity of DNA signal in the nuclear fragments of an apoptotic HeLa cell is $\sim$4–5$\times$ higher than that in the nucleus of a healthy HeLa cell (Fig. 9 *B*) and is approximately of the same level as encountered in measurements on fully mature PBL nuclei (Fig. 5 *A*). It has been proposed that the final level of condensation in an apoptotic cell is dramatic, exceeding the condensation observed in mitosis (Earnshaw, 1995). Present data show that at this stage of apoptosis, an appreciable condensation has taken place, but that this condensation gives rise to DNA concentrations still within the limits of what one may encounter under the physiological conditions in a different cell system. The line profiles through the image of DNA and protein distributions of the apoptotic nucleus with the corresponding SD are shown in Fig. 11, *D* and *E*, respectively. The arrow (Fig. 11, *B* and *C*) indicates the position in the cell nucleus corresponding with the line profile.

The protein Raman image of an apoptotic HeLa cell was reconstructed from the band $\sim$1451 cm^{-1} (spectral region

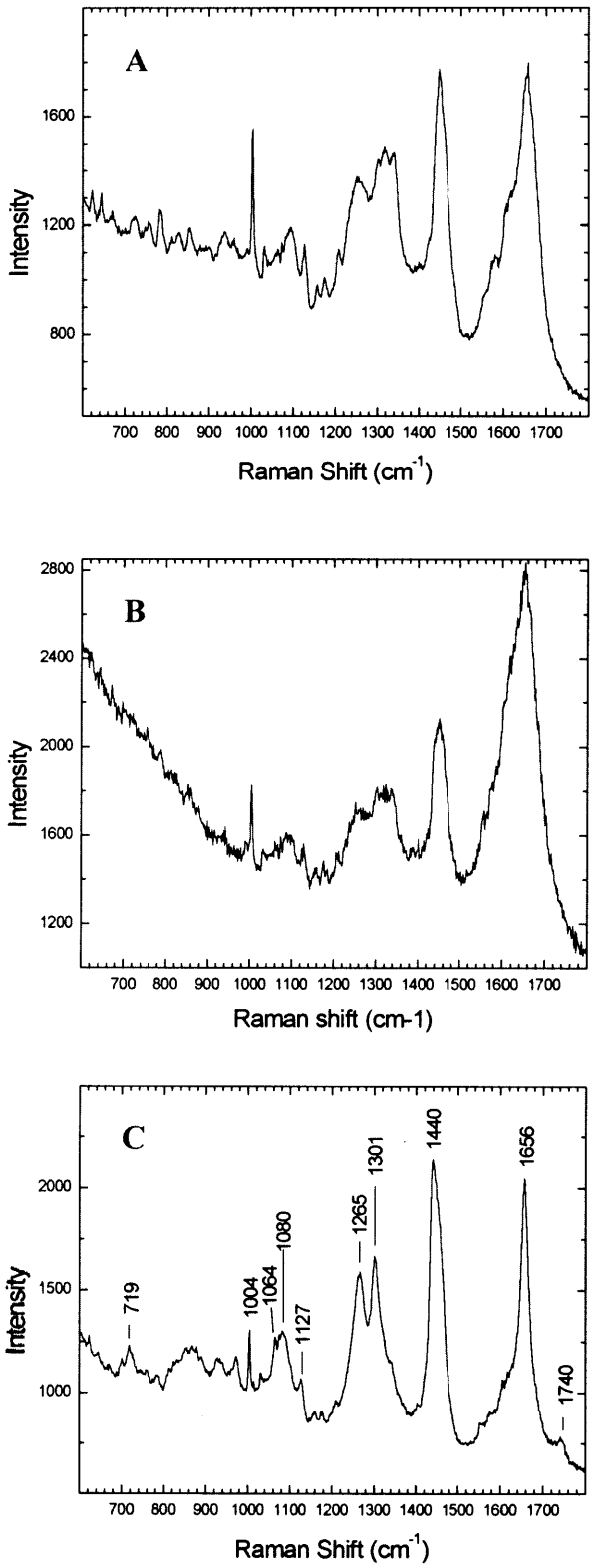

FIGURE 8 The Raman spectra obtained at the different locations inside a single fixed control HeLa cell. (*A*) The nucleus spectrum, average of seven spectra. (*B*) The cytosol spectrum, obtained at a single location. (*C*) The spectrum of the phospholipid-containing vesicles, average of five spectra. The cell was adhered to a CaF_2 disk, immersed in PBS buffer. The laser power was 100 mW, and the accumulation time was 60 s.

from 1434 cm^{-1} to 1474 cm^{-1}). Apparently (Fig. 11 *C*) the protein distribution is significantly different from the DNA distribution, although protein does occur in the regions of high nucleotide content. A few bright spots can be observed in Fig. 11 *C*. After inspection of the corresponding spectra, the observed particles can be ascribed to phospholipid-containing vesicles. Although some spectral variation occurs, we presently believe that these organelles are similar to those previously observed in control HeLa cells (Fig. 9 *C*). Alternatively, the spectra may also arise from mitochondria, from which, so far, no nonresonant Raman spectra have been published. Further research is in progress to distinguish cell organelles on the basis of Raman microspectroscopy and imaging.

CONCLUSIONS

We have demonstrated the application of nonresonant Raman imaging to visualize the DNA-, RNA-, protein-, and lipid distribution in human cells. This was accomplished by improvements in the choice of optical components in our homebuilt Raman microscope together with the use of high laser powers to compensate for the small nonresonant Raman scatter cross sections of the mentioned biological materials.

The effects of high laser powers on the chemical composition of the measurement volume have been assessed. Up to ~70 mW of laser power during 100 s at a wavelength of 647.1 nm gives rise to a single spectral component, as determined by singular value decomposition. The use of laser powers from 70 mW and higher during 100 s induces changes in the Raman spectrum resulting in a weak second spectral component as indicated by singular value decomposition. A conservative use of laser powers in the light of this assessment was selected to be 30 mW during 100 s for Raman microspectroscopy and 100 mW for up to 2 s for Raman imaging. Raman images were collected from the chemical distributions in peripheral blood lymphocytes as an example of a fully maturated cell. High quality images were obtained at a spatial interval of ~250 nm, i.e., a spatial frequency approximately 2× higher than the optical resolution of the Raman microscope.

The variations in the DNA and protein concentrations observed in the nucleus of the PBL cell can be related to the well-known heterochromatin and euchromatin areas. The variation in DNA signal is, however, more pronounced, indicating that an abundance of nonhistone proteins is present in heterochromatin area. It was established that the protein distribution obtained on the basis of the high frequency intense band between 2800 and 3030 cm^{-1} is identical to that obtained on the basis of the low frequency band between 1433 cm^{-1} and 1481 cm^{-1}. We have also shown that in mixed protein/lipid systems care has to be taken in the proper assignment of the 1450 cm^{-1} to either compound.

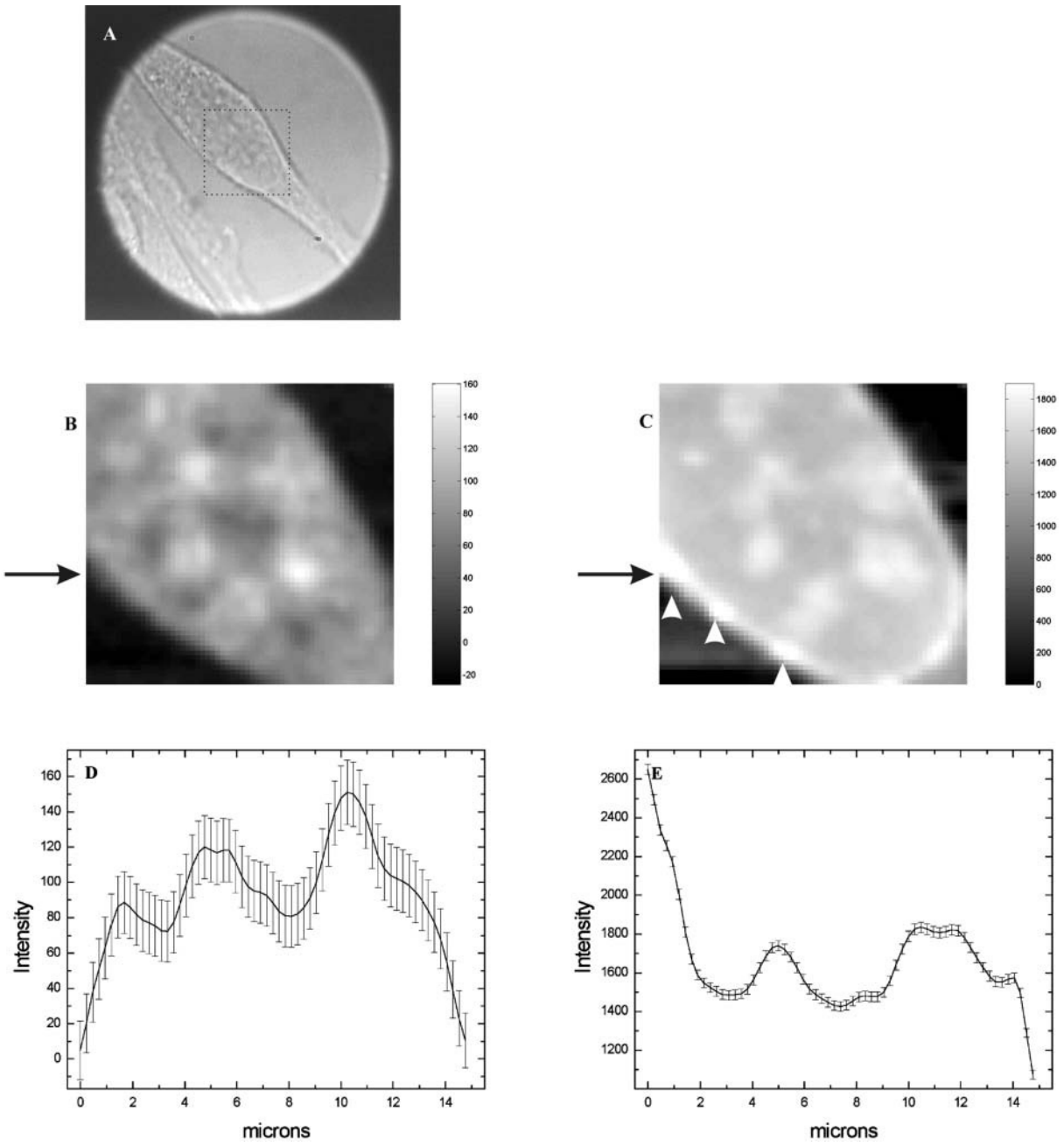

FIGURE 9 Raman imaging of a single fixed control HeLa cell. The cell was adhered to a CaF_2 disk, immersed in PBS buffer. (*A*) The bright light view of the cell. The dotted rectangle indicates the scanning area. (*B*) The image, reconstructed in 788 cm^{-1} band (spectral region from 776 cm^{-1} to 805 cm^{-1}). (*C*) Image, reconstructed in 1451 cm^{-1} band (spectral region from 1431 cm^{-1} to 1473 cm^{-1}). (*D*) The line profile through image *B* with the SD. (*E*) The line profile through image *C* with the SD. The SD intervals are shown as 2σ interval and were calculated using Eq. 2. The scanning area was 15 μm $\times$ 15 μm. The laser power was 100 mW, and the acquisition time was 2 s per step.

Raman imaging has been applied to investigate the chemical distribution of DNA, RNA, protein, and lipids in apoptotic cells. HeLa cells were incubated with taxol to induce apoptosis, and cells in a later stage of apoptosis were shown to have a high DNA content in nuclear fragments. Our direct method of chemical imaging shows that the DNA concentration in those fragments are much higher than found in the nuclei of control HeLa cells. However, the DNA concentration in the nuclear fragments corresponds roughly with that observed in fully maturated PBL cells, so that it must be concluded that no excessively high packaging of DNA at this stage of apoptosis is required (Earnshaw, 1995).

We also show, for the first time by Raman imaging and

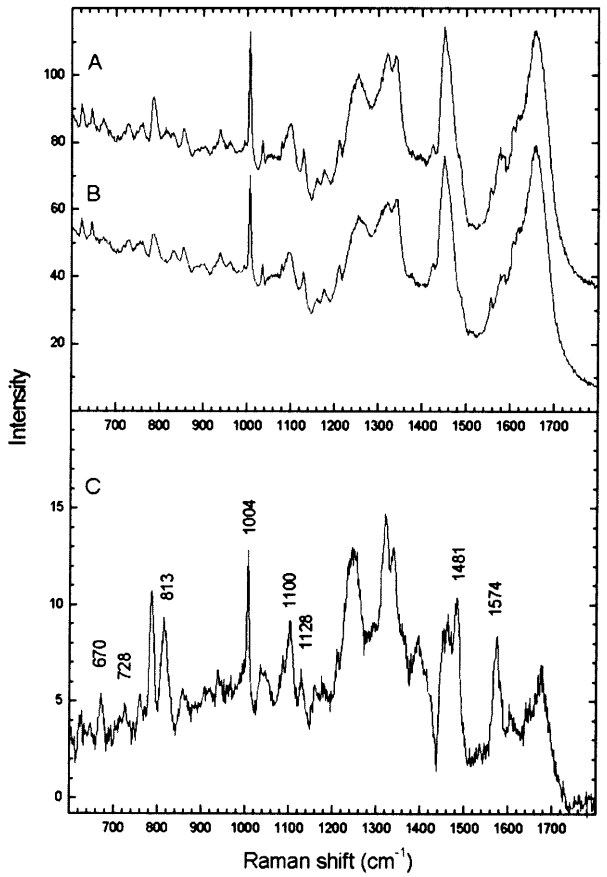

FIGURE 10 Average and difference Raman spectra obtained in a nucleus of the HeLa cell. (*A*) Average spectrum obtained from the bright intensity regions, visible in the image made in 788 cm^{-1} band. (*B*) Average spectrum obtained from the regions between the bright intensity regions. (*C*) Difference spectrum of *A* and *B*. Spectrum *A* was obtained by averaging of 41 individual spectra, and spectrum *B* by averaging of 103 individual spectra.

microspectroscopy, the presence of RNA in the HeLa cell nucleus.

The presence of lipid vesicles, probably components of the endosomal system, have been observed both in control and in apoptotic cells. This is especially of interest, since these particles could not be observed with white light microscopy as a result of the granular appearance of apoptotic cells.

We conclude that broad band (1800 cm^{-1}) spontaneous nonresonant Raman scattering is a powerful and versatile tool to investigate material distributions inside the cells. The high frequency resolution at which Raman images are obtained is of importance to distinguish between the various compounds inside the cell. The measurement time per pixel is of the order of 1 s. The use of statistical methods to reduce noise is a requirement. We have used singular value decomposition for this purpose, which demands no input from the user and is a generally available tool that is easy to use.

APPENDIX A

In Raman measurements four dominant noise components can be distinguished: shot noise, dark current noise, readout noise, and processing noise. Shot noise refers to the inherent natural variation of the incident photon flux. The detector itself also contributes to the total noise. For a liquid nitrogen-cooled CCD camera (LN/CCD 1100 PB/VISAR, Roper Scientific, Trenton, NJ), the sources of noise are: 1), the dark noise, originating from the statistical variation of the thermally generated electrons within a silicon layer comprising the CCD; and 2), the readout noise, arising from the uncertainty introduced by the process of quantifying the electrons on the CCD. The major component of the latter arises from the on-chip preamplifier. The specified numbers (from data sheet of Roper Scientific) for the dark current is 0.5 electrons per pixel per h, at $-100°C$; and for the readout noise, seven electrons per readout, at 50 kHz readout rate (for the LN/CCD 1100 PB/VISAR, Roper Scientific). Usually the CCD dark current noise is negligibly small in comparison to the shot noise. However, the readout noise can make considerable contribution to the total noise level. The light source used for excitation may potentially also introduce noise. The specified value for the long term power stability (over ~30 min) of the 90-K laser is 0.5%. Basic data processing such as the background subtraction and correction of the data for the setup throughput (Puppels et al., 1991a) also results in unavoidable increase of the amount of noise. The calculated error intervals (as given in Fig. 5, *C*, *D*, and *F*; Fig. 9, *D* and *E*; and Fig. 11, *D* and *E*) contain all relevant noise parameters.

APPENDIX B

The basic concepts of singular value decomposition are described in detail in a study by Golub and van Loan (1983). The theorem for singular value decomposition is stated in mathematical terms as:

$$\mathbf{A} = \mathbf{U}\mathbf{S}\mathbf{V}^{\mathrm{T}}$$
$$\mathbf{U}\mathbf{U}^{\mathrm{T}} = \mathbf{I}_{\mathrm{n}}, \quad \mathbf{V}\mathbf{V}^{\mathrm{T}} = \mathbf{I}_{\mathrm{n}},$$

where $\mathbf{I}_{\mathrm{n}}$ is the identity matrix.

According to this theorem, any matrix $\mathbf{A}$ can be decomposed into three matrices. The first one, matrix $\mathbf{U}$, is orthonormal and spans up the column space of $\mathbf{A}$. The matrix $\mathbf{V}$ is orthonormal and spans up the row space of $\mathbf{A}$. The matrix $\mathbf{S}$ is a diagonal matrix:

$$S_{\mathrm{ij}} = \begin{cases} \sigma_{\mathrm{i}} & 1 \le i = j \le n \\ 0, & \text{otherwise} \end{cases},$$

with $\sigma_1 \ge \sigma_2 \ge \ldots \sigma_{\mathrm{n}} \ge 0$, the so-called singular values of $\mathbf{A}$.

After rejection of the singular values belonging to the noise and reconstruction back of a new data matrix $\tilde{\mathbf{A}}$, the spectral data set effectively contains less noise. We can approximate the original matrix $\mathbf{A}$ by a matrix of rank n_{dim} given by:

$$\tilde{\mathbf{A}} = \mathbf{U}\tilde{\mathbf{S}}\mathbf{V}^{\mathrm{T}},$$

with

$$\tilde{\sigma}_{\mathrm{i}} = \begin{cases} \sigma_{\mathrm{i}} & 1 \le i \le n_{\mathrm{dim}} \\ 0, & n_{\mathrm{dim}} + 1 \le i \le n \end{cases}.$$

The square approximation error is given by

$$\|\tilde{\mathbf{A}} - \mathbf{A}\|_{\mathrm{F}}^2 = \sum_{\mathrm{i}=1}^{\mathrm{m}} \sum_{\mathrm{j}=1}^{\mathrm{n}} (\tilde{A}_{\mathrm{ij}} - A_{\mathrm{ij}})^2 = \sum_{\mathrm{i}=\mathrm{n}_{\mathrm{dim}}+1}^{\mathrm{n}} \sigma_{\mathrm{i}}^2.$$

With $n_{\mathrm{dim}} = 10$ we have a relative square approximation error of no more then 0.5% for the available data. Thus, SVD itself acts as an efficient

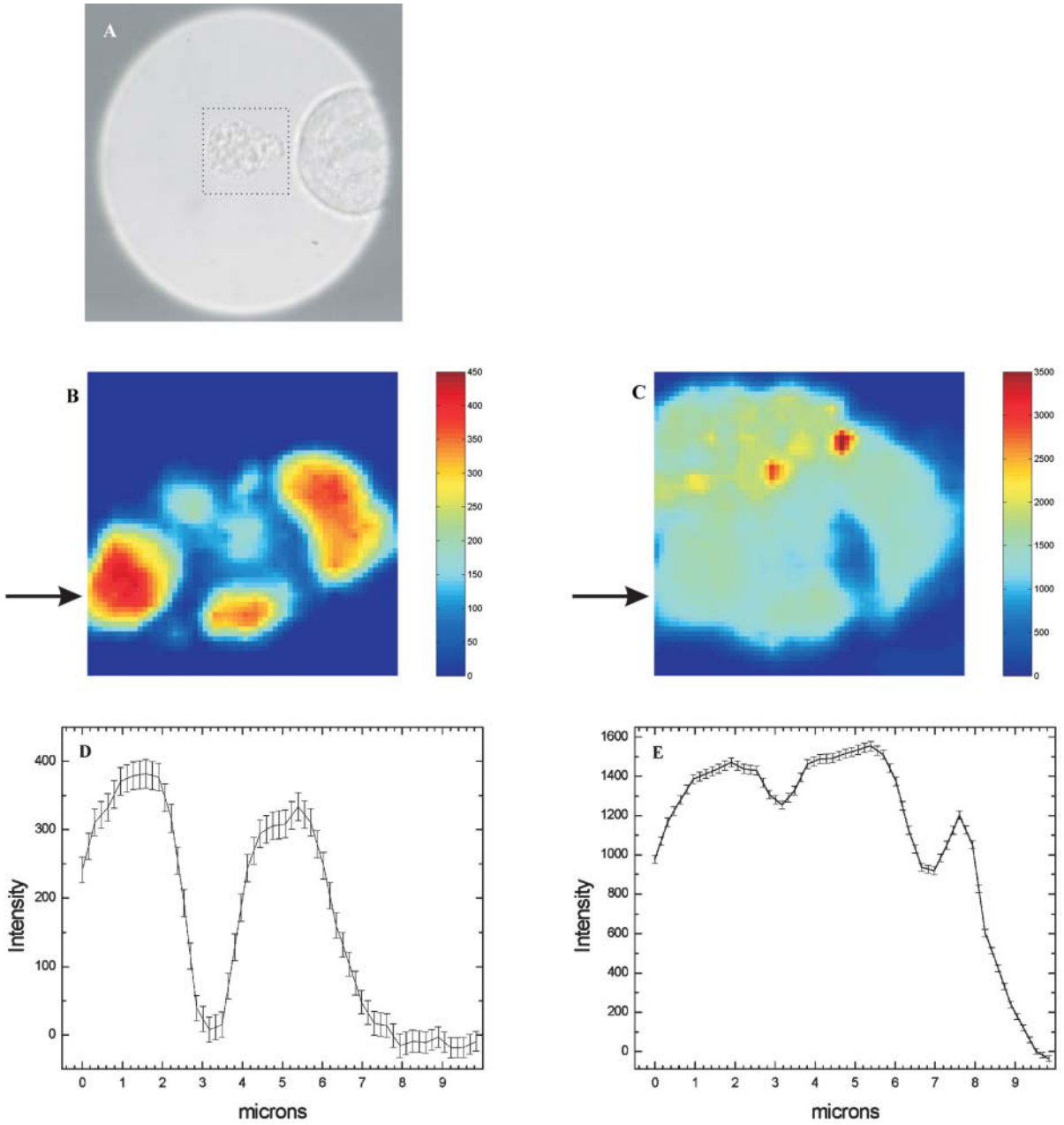

FIGURE 11 Raman imaging of a single fixed apoptotic HeLa cell. The cell was adhered to a CaF_2 disk, immersed in PBS buffer. (*A*) A bright light view of the cell. The dotted rectangle indicates the scanning area. (*B*) DNA image, reconstructed in 788 cm^{-1} band (spectral region from 774 cm^{-1} to 805 cm^{-1}). (*C*) Protein image, reconstructed in 1451 cm^{-1} band (spectral region from 1434 cm^{-1} to 1474 cm^{-1}). (*D*) Line profile with the SD through the DNA image. (*E*) Line profile with the SD through the protein image. The SD intervals are shown as 2σ interval, and were calculated using Eq. 2. The background intensity due to the Raman scattering of water and the camera offset was subtracted. The scanning area was 10 μm $\times$ 10 μm. The laser power was 100 mW, and the acquisition time was 1 s per step.

filter to suppress random noise in the most significant components. A data set reconstructed from the SVD components is therefore effectively noise-filtered without the artifacts that may arise when some of the more popular smoothing algorithms are used (Henry and Hofrichter, 1992).

The relevant singular values are chosen using criteria described previously (Hag et al., 1997). Singular value decomposition of two-dimensional data matrix was done using the program MATLAB (The Mathworks, Natick, MA).

REFERENCES

Arikan, S., H. S. Sands, R. G. Rodway, and D. N. Batchelder. 2002. Raman spectroscopy and imaging of beta-carotene in live corpus luteum cells. *Anim. Reprod. Sci.* 71:249–266.

Biggiogera, M., M. G. Bottone, and C. Pellicciari. 1998. Nuclear RNA is extruded from apoptotic cells. *J. Histochem. Cytochem.* 46:999–1005.

Byassee, T. A., W. C. Chan, and S. Nie. 2000. Probing single molecules in single living cells. *Anal. Chem.* 72:5606–5611.

Cheng, J.-X., A. Volkmer, L. D. Book, and X. S. Xie. 2001. An epi-detected anti-Stokes Raman scattering (E-CARS) microscope with high spectral resolution and high sensitivity. *J. Phys. Chem. B*. 105:1277–1280.

Cheng, J.-X., A. Volkmer, L. D. Book, and X. S. Xie. 2002. Multiplex coherent anti-Stokes Raman scattering microspectroscopy and study of lipid vesicles. *J. Phys. Chem. B*. 106:8493–8498.

Compton, M. M. 1992. A biochemical hallmark of apoptosis: internucleosomal degradation and removal by macrophages. *J. Immunol*. 148:2207–2216.

Darzynkiewicz, Z. 1990. Probing nuclear chromatin by flow cytometry. *In* Flow Cytometry and Sorting. M. R. Melamed, T. Lindmo, and M. L. Mendelsohn, editors. Wiley-Liss, Inc., New York, NY. pp. 315–340.

Deng, H., V. A. Bloomfield, J. M. Benevides, and G. J. Thomas, Jr. 1999. Dependence of the Raman signature of genomic B-DNA on nucleotide base sequence. *Biopolymers*. 50:656–666.

Diem, M., L. Chiriboga, P. Lasch, and A. Pacifico. 2002. IR spectra and IR spectral maps of individual normal and cancerous cells. *Biopolymers*. 67:349–353.

Dundr, M., and T. Misteli. 2001. Functional architecture in the cell nucleus. *Biochem. J*. 356:297–310.

Earnshaw, W. C. 1995. Nuclear changes in apoptosis. *Curr. Opin. Cell Biol*. 7:337–343.

Golub, G. H., and C. F. van Loan. 1983. Matrix Computations. North Oxford Academic Publishing, Oxford.

Hag, I., B. Z. Chowdhry, and J. B. Chaires. 1997. Singular value decomposition of 3-D melting curves reveals complexity in the melting process. *Eur. Biophys. J*. 26:419–426.

Halicka, H. D., E. Bedner, and Z. Darzynkiewicz. 2000. Segregation of RNA and separate packaging of DNA and RNA in apoptotic bodies during apoptosis. *Exp. Cell Res*. 260:248–256.

Hartman, K. A., and G. J. Thomas. 1985. The identification, interactions and structure of viruses by Raman spectroscopy. *In* Instrumental Methods for Rapid Microbiological Analysis. W. H. Nelson, editor. VCH Publishers, Deerfield Beach, FL. pp. 91–134.

Hayashi, H., Y. Nishimura, M. Katahira, and M. Tsuboi. 1986. The structure of nucleosome core particles as revealed by difference Raman spectroscopy. *Nucleic Acids Res*. 14:2583–2596.

van der Heijden, F. 1994. Image-Based Measurements Systems—Object Recognition and Parameter Estimation. Wiley & Sons, New York.

Hell, S. W., M. Booth, and S. Wilms. 1998. Two-photon near- and far-field fluorescence microscopy with continuous-wave excitation. *Optics Lett*. 23:1238–1240.

Henry, E. R., and J. Hofrichter. 1992. Singular value decomposition—application to analysis of experimental data. *Method. Enzymol*. 210: 129–192.

Houge, G., B. Robaye, T. S. Eikhom, J. Golstein, G. Mellgren, B. T. Gjertsen, M. Lanotte, and S. O. Doskeland. 1995. Fine mapping of 28S rRNA sites specifically cleaved in cells undergoing apoptosis. *Mol. Cell. Biol*. 15:2051–2062.

Iino, R., R. Koyama, and A. Kusumi. 2001. Single molecule imaging of green fluorescent proteins in living cells: E-cadherin forms oligomers on the free cell surface. *Biophys. J*. 80:2667–2677.

Kerr, J. F. R., A. H. Wyllie, and A. R. Curie. 1972. Apoptosis: a basic biological phenomenon with wide-range implications in tissue kinetics. *Br. J. Cancer*. 26:239–257.

Kerr, J. F., C. M. Winterford, and B. V. Harmon. 1994. Apoptosis. Its significance in cancer and cancer therapy. *Cancer*. 73:2013–2026.

Kirsch, A. K., V. Subramanian, G. Striker, C. Schnetter, D. J. Arndt-Jovin, and T. M. Jovin. 1998. Continuous wave two-photon scanning near-field optical microscopy. *Biophys. J*. 75:1513–1521.

Lasch, P., A. Pacifico, and M. Diem. 2002. Spatially resolved IR microspectroscopy of single cells. *Biopolymers*. 67:335–338.

Lim, S.-N., F. Bonzelius, S. H. Low, H. Wille, T. Weimbs, and G. Herman. 2001. Identification of discrete classes of endosome-derived small vesicles as a major cellular pool for recycling membrane proteins. *Mol. Biol. Cell*. 12:981–995.

Loontiens, F. G., P. Regenfuss, A. Zechel, L. Dumortier, and R. M. Clegg. 1990. Binding characteristics of Hoechst 33258 with calf thymus DNA, poly[d(A-T)], and d(CCGGAATTCCGG): multiple stoichiometries and determination of tight binding with a wide spectrum of site affinities. *Biochemistry*. 29:9029–9039.

Majno, G., and I. Joris. 1995. Apoptosis, oncosis, and necrosis. An overview of cell death. *Am. J. Pathol*. 146:3–16.

Nagata, S. 2000. Apoptotic DNA fragmentation. *Exp. Cell Res*. 256:12–18.

Otto, C., N. M. Sijtsema, and J. Greve. 1998. Confocal Raman microspectroscopy of the activation of single neutrophilic granulocytes. *Eur. Biophys. J*. 27:582–589.

Peticolas, W. L., W. L. Kubasek, G. A. Thomas, and M. Tsuboi. 1987. Biological Applications of Raman Spectroscopy. T. G. Spiro, editor. Wiley & Sons, New York. pp. 81–133.

Puppels, G. J., W. Colier, J. H. F. Olminkof, C. Otto, F. F. M. de Mul, and J. Greve. 1991a. Description and performance of a highly sensitive confocal Raman microscope. *J. Raman Spectrosc*. 22:217–225.

Puppels, G. J., H. S. P. Garritsen, G. M. J. Segers-Nolten, F. F. M. de Mul, and J. Greve. 1991b. Raman microspectroscopic approach to the study of human granulocytes. *Biophys. J*. 60:1046–1056.

Puppels, G. J., H. S. P. Garritsen, J. A. Kummer, and J. Greve. 1993a. Carotenoids located in human lymphocyte subpopulations and natural-killer cells by Raman microspectroscopy. *Cytometry*. 14:251–256.

Puppels, G. J., M. van Rooijen, C. Otto, and J. Greve. 1993b. Fluorescent and Luminescent Probes. W.T. Mason, editor. Academic Press, London. pp. 238–258.

Puppels, G. J., F. F. M. de Mul, C. Otto, J. Greve, M. Robert-Nicoud, D. J. Arndt-Jovin, and T. M. Jovin. 1990. Studying single living cells and chromosomes by confocal Raman microspectroscopy. *Nature*. 347:301–303.

Puppels, G. J., C. Otto, J. Greve, M. Robert-Nicoud, D. J. Arndt-Jovin, and T. M. Jovin. 1994. Raman microspectroscopic study of low-pH-induced changes in DNA structure of polytene chromosomes. *Biochemistry*. 33:3386–3395.

Ramanauskaite, R. B., G. M. J. Segers-Nolten, K. J. de Graw, N. M. Sijtsema, L. van der Maas, J. Greve, C. Otto, and C. G. Fidgor. 1997. Carotenoid levels in human lymphocytes, measured by Raman microspectroscopy. *Pure Appl. Chem*. 69:2131–2134.

Robertson, J. D., S. Orrenius, and B. Zhivotovsky. 2000. Review: nuclear events in apoptosis. *J. Struct. Biol*. 129:346–358.

Salmaso, B. L., G. J. Puppels, P. J. Caspers, R. Floris, R. Wever, and J. Greve. 1994. Resonance Raman microspectroscopic characterization of eosinophil peroxidase in human eosinophilic granulocytes. *Biophys. J*. 67:436–446.

Schuster, K. C., I. Reese, E. Urlaub, J. R. Gapes, and B. Lendl. 2000. Multidimensional information on the composition of single bacterial cells by confocal Raman microspectroscopy. *Anal. Chem*. 72:5529–5534.

Schwartz, L. M., and B. A. Osborne. 1993. Programmed cell death, apoptosis and killer genes. *Immunol. Today*. 14:582–590.

Sijtsema, N. M., C. Otto, G. M. J. Segers-Nolten, A. J. Verhoeven, and J. Greve. 1998a. Resonance Raman microspectroscopy of myeloperoxidase and cytochrome b(558) in human neutrophilic granulocytes. *Biophys. J*. 74:3250–3255.

Sijtsema, N. M., S. D. Wouters, C. J. de Grauw, C. Otto, and J. Greve. 1998b. Confocal direct imaging Raman microscope: design and applications in biology. *Appl. Spectrosc*. 52:348–355.

Sijtsema, N. M., A. G. J. Tibbe, G. M. J. Segers-Nolten, A. J. Verhoeven, R. S. Weening, J. Greve, and C. Otto. 2000. Intracellular reactions in single human granulocytes upon phorbol myristate acetate activation using confocal Raman microspectroscopy. *Biophys. J*. 78:2606–2613.

Terstappen, L. W., B. G. de Grooth, G. M. J. Segers-Nolten, C. H. ten Napel, W. van Berkel, and J. Greve.1986. Physical discrimination between human T-lymphocyte subpopulations by means of light

scattering, revealing two populations of T8-positive cells. *Cytometry*. 7:178–183.

Thomas, G. J., Jr., B. Prescott, and D. E. Olins. 1977. Secondary structure of histones and DNA in chromatin. *Science*. 197:385–388.

Thomas, G. J., Jr., B. Prescott, and L. A. Day. 1983. Structure similarity, difference and variability in the filamentous viruses fd, If1, IKe, Pf1, Xf and Pf3. *J. Mol. Biol.* 165:321–356.

Tu, A. T. 1982. Raman Spectroscopy in Biology: Principles and Application. Wiley, New York.

Uzunbajakava, N., A. Lenferink, Y. Kraan, B. Willekens, G. Vrensen, J. Greve, and C. Otto. 2003. Nonresonant Raman imaging of protein distribution in single human cells. *Biopolymers*. 72:1–9.

Verschure, P. J., I. van der Kraan, E. M. M. Manders, and R. van Driel. 1999. Spatial relationship between transcription sites and chromosome territories. *J. Cell Biol.* 147:13–24.

Volkmer, A., J.-X. Cheng, and X. S. Xie. 2001. Vibrational imaging with a high sensitivity via epidetected coherent anti-Stokes Raman scattering microscopy. *Phys. Rev. Lett*. 87:023901.

Wyllie, A. H. 1992. Apoptosis and regulation of cell numbers in normal and neoplastic tissues: an overview. *Cancer Metastasis Rev*. 11:95–103.

Wood, B. R., B. Tait, and D. McNauton. 2001. Micro-Raman characterization of the R to T state within a single living erythrocyte. *Biochim. Biophys. Acta*. 1539:58–70.

Yeung, T. K., C. Germond, X. Chen, and Z. Wang. 1999. The mode of action of Taxol: apoptosis at low concentration and necrosis at high concentration. *Biochem. Biophys. Res*. 263:398–404.

Zucker-Franklin, D., M. F. Greaves, C. E. Grossi, and A. M. Marmont. 1988. Atlas of Blood Cells: Function and Pathology. Edi. Ermes, Milano.

Zumbusch, A., G. R. Holtom, and X. S. Xie. 1999. Three-dimensional vibrational imaging by coherent anti-Stokes Raman scattering. *Phys. Rev. Lett*. 82:4142–4145.